APEM journal
Advances in Production Engineering & Management
Volume 21 | Number 2 | June 2026 | pp 254–267
https://doi.org/10.14743/apem2026.2.572
ISSN 1854-6250
Journal home: apem-journal.org
Original scientific paper

Microstructure-based multiscale prediction of pruning cutter wedge angle for jujube branches

Zhang, S.[a], Wu, S.H.[b,*], Chen, C.[a], Huang, C.L.[a], Jiang, T.T.[a], Zhao, C.L.[a,c], Zhao, Y.H.[c,d], Ciwang, L.[c]

[a]Geely University of China, Chengdu, P.R. China
[b]Sichuan Technology & Business College, Chengdu, P.R. China
[c]Xizang University, Lhasa, P.R. China
[d]Xizang Hydraulic and Electric Planning, Survey and Design Institute, Lhasa, P.R. China

A B S T R A C T

The biomechanical properties of jujube branches constitute fundamental parameters for evaluating cutting performance of pruning machinery and optimizing the wedge angle of cutting tools. To investigate how microstructural heterogeneity across different branch regions influences cutting behavior, we integrated X-ray CT imaging with nanoindentation testing. Representative volume elements (RVEs) were constructed from experimentally resolved microstructures to enable multiscale finite element modeling of the pruning process, thereby revealing microscale mechanisms governing cutting resistance. Microstructural characteristics—including porosity, cell wall thickness, and water content—were quantified across five positions along the branch, and their effects on the homogenized (equivalent) shear modulus were systematically evaluated. Results show that both increasing porosity and elevated water content significantly reduce the equivalent shear modulus, with porosity exhibiting a markedly stronger attenuating effect. Crucially, the recommended wedge angle is governed primarily by the ratio of longitudinal-to-transverse shear modulus; based on mechanical sensitivity analysis, the recommended design angle is α = 21.75°. This study provides a biomechanical basis for the rational design and performance optimization of specialized pruning tools for jujube trees.

A R T I C L E I N F O

Keywords:
Jujube branch;
Nanoindentation;
X-ray computed tomography;
Representative volume element;
Multiscale finite element analysis;
Cutting wedge angle;
Pruning machinery

**Corresponding author:*
1529432209@qq.com
(Wu, S.H.)

Article history:
Received 9 September 2025
Revised 3 July 2026
Accepted 7 July 2026

1. Introduction

Chinese jujube (Ziziphus jujuba Mill) is a type of deciduous tree of the buckthorn family with origins in China. Jujube production in Xinjiang, the largest jujube production area in China, exceeded 560,000 tons in 2024. Trimming and shaking operations during orchard production are important aspects for tree management and improving jujube yield. Microstructures largely determine the mechanical properties of jujube branches and affect trimming and shaking machine operations, such as cutting energy consumption and cutting angle. A comprehensive understanding of the internal relationship between microstructure and mechanical properties of jujube branches is of great significance for selecting a suitable pruning position and cutting wedge angle, and improving the working performance of pruning machinery. In response to the above issues, the main work of this paper is as follows:

- The micro-mechanical properties of the cell walls of jujube branches were studied by pressing a nanoindenter into the sample surface. Industrial CT was used for X-ray scanning to reconstruct a microstructural visualization model. Based on the binary image results, quantitative analysis methods were employed to obtain the characteristics of different microscopic components.
- Based on the results of micro-mechanical analysis and the reconstructed microscopic structure, the constraint equations of the representative volume element under uniaxial compression and shear displacement loads were established to analyze the multi-scale mechanical properties of the microscopic structure. Finite element analysis was conducted using Abaqus, and the recommended pruning position and cutting wedge angle were determined from the analysis results.

2. Related work

Jujube trees are an important economic crop in Xinjiang, China. Promoting the mechanization and intelligence of jujube tree planting is of great significance in terms of improving production efficiency, reducing costs, enhancing quality, and promoting the sustainable development of the industry. Most of the related research focuses on machine vision technology and covers all growth stages of jujube trees. During the harvesting stage, Zheng *et al.* designed a visual perception system for the trunk and branches of jujube trees, including trunk and branch detection, skeleton extraction, and confirmation of the grasping and shaking areas. This system can identify an unobstructed area for grasping and shaking and guide the mechanical arm to reach this area to complete the harvesting operation. Considering the complex orchard environment and numerous interfering factors, a low-cost vision system based on convolutional neural networks and machine learning algorithms was proposed to obtain an accurate navigation path for the grasping and shaking harvesting robot in the winter jujube orchard [1-2]. Path planning and obstacle avoidance are also key components of autonomous mobile robot navigation in complex environments [3]. Hu *et al.* noted that if the vibration frequency is too high, it will cause damage to jujube trees, and if it is too low, it will be impossible to separate the fruit from the fruit stalks, leading to a failed harvest. They used the finite element method and vibration tests to find the optimal vibration parameters. To enhance the accuracy of the finite element method, they conducted modal analysis to determine the natural frequency of the jujube tree and applied transient analysis to study the vibration transmission characteristics [4]. Zheng *et al.* addressed the lack of precise three-dimensional tree models for studying the vibration characteristics of different fruit trees based on the finite element method. They utilized multi-view 3D reconstruction technology to obtain accurate three-dimensional tree models for simulation analysis. They carried out transient analysis and test experiments to explore the energy transmission characteristics at different vibration frequencies [5].

During the pruning stage, a pruning point identification method based on skeleton information can be used for automatic pruning of jujube trees. Semantic segmentation methods can be used to extract relevant structural information from complex images [6]. The method generates the jujube tree skeleton by applying the spatial colonization algorithm to the global point cloud, and represents the iterative relationship between the skeleton points by constructing a directed graph. Deep-learning-based object detection methods, including different YOLO architectures, have also been successfully applied to complex visual detection and classification tasks [7-8]. Such approaches provide useful methodological support for the detection of tree trunks and branches in complex orchard environments. Improved multi-view stereo methods combined with remote sensing and artificial intelligence can support the reconstruction of orchard fruit trees. In view of the complex environment and large data flow of orchards, the existing target detection schemes have problems such as poor data quality, low timeliness and accuracy, and weak generalization ability. YOLO-based models can enable lightweight and accurate detection of jujube tree trunks.

During the growth stage, Peng *et al.* proposed a branch model based on turtle interpretation, which simulated the curved shape of jujube branches, enhanced the three-dimensional visualization effect, and effectively simulated the morphological structure of jujube trees. Subsequently, a new L-system for jujube visualization based on a substructure algorithm was developed, which could control the morphological structure and growth process of jujubes through relevant parameter settings [9]. Ma *et al.* studied the detection method of water deficiency in jujube tree canopies based on spectral technology and proposed a detection method combining fractal theory. First, the fractal dimensions of each spectral curve of the water-deficient canopy and the healthy canopy after preprocessing were calculated, and it was found that the fractal dimension of the healthy state was greater than that of the water-deficient state; the fractal features of spectral data, spectral feature parameters and principal components of spectra were used as feature vectors, and binary classification was performed based on the random forest algorithm [10]. For the classification of jujube fruit, Mahmood *et al.* developed an efficient and reliable jujube grading model. They utilized MVS for jujube image acquisition, followed by image preprocessing and enhancement tasks. By using the Adam optimizer, they achieved a maximum success rate of 99.44 % (i.e., an error of 0.56 %) in grading [11]. Zhang *et al.* noted that jujubes are susceptible to biotic and abiotic stress, leading to abnormal phenotypic defects. They developed an improved maximum horizontal diameter linear regression (MHD-LR) method for size grading of jujubes before detecting abnormal phenotypic defects. This method can effectively and accurately classify seven types of jujube phenotypes (regular type, irregular type, wrinkled type, moldy type, perforated type, cracked type, and scarred type) [12].

Apart from the research on jujube trees, there is also a considerable amount of research on other fruit trees. Qiu *et al.* proposed a high-precision branch extraction process through the alignment of point clouds at different times for the dormant pruning mode of apple trees, achieving quantitative analysis of the pruning mode. They conducted a feature analysis on the structural parameters of 126 pear trees during the entire growth period, and the research results showed that the structure of the trees had a greater impact on pruning than the cultivar, especially in Cuiguan, where significant differences were observed among different tree structures [13]. Tong *et al.* proposed an intelligent fruit tree pruning robot system suitable for tall spindle apple trees. The system consists of a visual system, a pruning decision system, and a robotic arm with an end effector control system. The visual system is used for apple branch segmentation and adopts the SOLOv2 Swin algorithm to achieve a maximum mAP50 segmentation accuracy of 0.941. Compared with other segmentation algorithms, this method significantly improves the accuracy and performance of segmentation [14]. Liu *et al.* addressed the issue that the vibration harvesting efficiency of forest fruits such as camellia flowers depends on the machine vibration parameters and the biomechanics of the trees. Based on the dynamic branch and fruit model of the external body trajectory, they determined the excitation frequency and trajectory amplitude as the key factors for detachment. They formulated an optimal pruning plan to facilitate harvesting while reducing yield. The average fruit removal rate in the field harvesting experiment was 75.1 %, and the average flower bud shedding rate was 11.6 % [15]. Cao *et al.* proposed a new adaptive rectangular region growth segmentation algorithm to solve the problem of precise segmentation of tree trunks and branches. This method combines an adaptive growth carrier based on the growth trend of branches and a dynamic growth rectangular region adjusted according to the diameter of branches. An innovative reverse growth strategy was also introduced to enhance the efficiency of the growth process. This algorithm can automatically and effectively identify the starting and ending points of growth based on the structural characteristics of the fruit tree branches, solving the problem of where to start and when to stop [16].

Win *et al.* evaluated the effects of mechanical pruning on the growth, yield, and fruit quality of "Arisoo" apple trees over two consecutive years (2023 and 2024). The treatment methods included manual pruning, mechanical pruning, and the combination of mechanical and manual pruning during the winter pruning period in the super-long apple orchard. Overall, the study found that mechanical pruning reduced light penetration, resulting in smaller fruits with poorer color, while the subsequent combination of mechanical and manual pruning improved pruning efficiency, light penetration, fruit size, and fruit quality [17]. Chen *et al.* proposed an improved bidirectional rapid expansion random tree (RRT-Connect) algorithm to enable fruit-tree pruning manipulators to avoid obstacles in unstructured and complex natural environments. The mechanical arms and obstacles were appropriately simplified based on their geometric characteristics to construct a collision detection model considering obstacles, the ground, and the mechanical arms themselves, and to plan paths for obstacle avoidance. The target bias strategy and adaptive step size adjustment principle were introduced to accelerate the path search speed. The bidirectional pruning optimal strategy and the cubic non-uniform B-spline interpolation method were adopted to optimize the path generated by RRT-Connect [18]. Liu *et al.* applied robotic manipulators to the automated solution for apple tree pruning, proposed the planning problem of high-dimensional mechanical arms in the pruning scenario, studied the inherent redundancy of the system, and proposed a comprehensive pruning workflow integrating perception, modeling, and overall planning. The experiments showed that a more comprehensive planning method could significantly improve manipulator performance [19].

3. Materials and methods

The dwarf and densely planted jujube trees in Alar City of Xinjiang were used as experimental materials (variety: Junyou; age: 6 years; diameter: 8-20 mm). Mature jujube branches were randomly sampled. Based on branch length, the branches were divided into five sections from the base upwards (Fig. 1) to analyze the differences in properties such as porosity and water content [20-22].

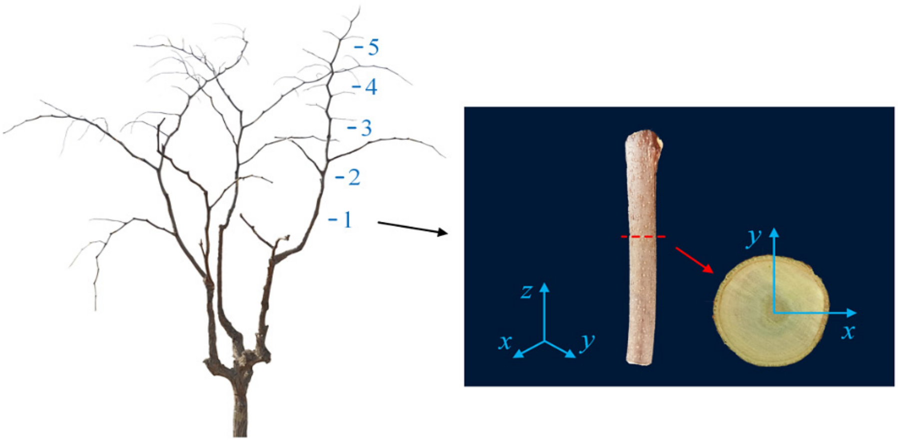

Fig. 1 Experimental samples of jujube branch

3.1 Mechanical properties of the cell wall

Nanoindentation technology uses an indenter tip pressed into the sample surface to produce small elastic deformations and measure the micromechanical properties, such as elastic modulus, hardness, and viscoelasticity. The cell wall is the main carrier of the stem that bears the external load. The cell wall is mainly composed of an intercellular layer and primary and secondary walls, and the thickness of the secondary wall layer accounts for 80 % of the entire wall thickness. Micromechanical tests were therefore only carried out on the secondary wall in this study [23-24].

Related studies show that plant cell walls are transversely isotropic materials [25-26]. The direction along the branch striations was defined as the z-direction (longitudinal), while the x- and y-directions were defined as transverse directions; the xy-plane was therefore treated as transversely isotropic. The samples were shaped into pyramids of different sizes according to branch diameter and cut into 0.5 × 0.5 mm areas at the pyramid apex using an ultra-thin slicer (Fig. 2a, 2b). Four test areas were selected on the sample surface using a Hysitron TI-950 nanoindenter (Fig. 2b, 2c) and optical microscope with 10 indentation points for each area (Fig. 2d, 2e). The longitudinal mechanical properties of the cell wall were measured under a 90 μN load and an indentation depth of 60-90 nm. Three samples were randomly selected, with 40 indentation points on each sample.

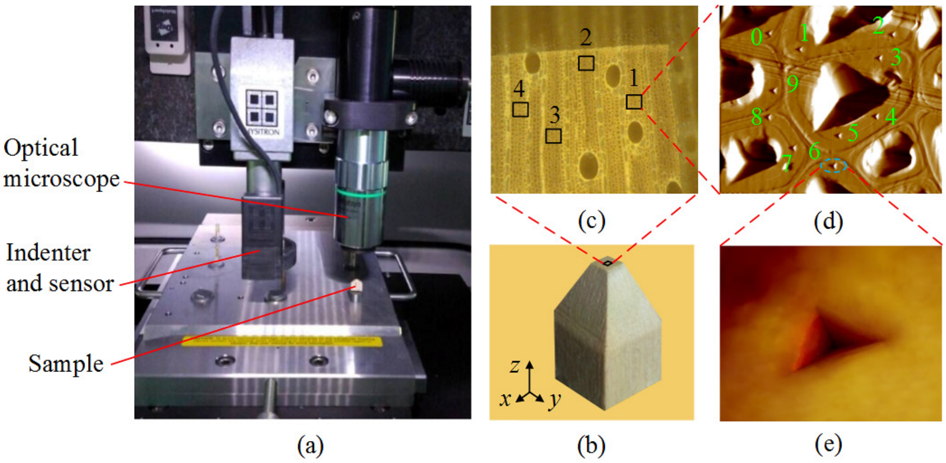

Fig. 2 Nano-indentation test of the cell wall: (a) nanoindentation instrument; (b) sample; (c) test area; (d) indentation area; (e) indentation morphology

The reduced elastic modulus E_r was calculated from the nanoindentation data using Eq. 1:

$$E_r = \frac{\sqrt{\pi}}{2\beta}\frac{S}{\sqrt{A}} \tag{1}$$

where E_r is the reduced elastic modulus of the sample, MPa. β is a constant related to the Berkovich indenter geometry and has a value of 1.034. S is the contact stiffness, μN/nm. A is the contact area between the indenter and sample, nm^2. The elastic modulus E_s of the sample was then calculated from the reduced elastic modulus using Eq. 2:

$$\frac{1}{E_r} = \frac{1-\mu_s^2}{E_s} + \frac{1-\mu_i^2}{E_i} \tag{2}$$

where μ_s is the Poisson's ratio of the sample, with a value of 0.15-0.35. E_s is the elastic modulus of the sample, MPa. E_i is the elastic modulus of the diamond indenter and has a value of 1.141 × 10^6 MPa. μ_i is the Poisson's ratio of the diamond indenter and has a value of 0.07. Because the longitudinal elastic modulus (E_z) of the cell wall inside the wood is 3.5-10 times higher than the transverse elastic modulus, $E_s = E_z$. In this study, E_z is 6.75 times higher than the calculated average transverse elastic modulus E_x. Because the Poisson's ratio of the wood has little effect on its elastic parameters, the Poisson's ratio of the cell wall was selected as μ_{xy} = 0.24 with a reference value of μ_{zx} = 0.1. The in-plane transverse shear modulus G_{xy} of the cell wall was calculated using $G_{xy} = E_x/[2(1+\mu_{xy})]$, while the longitudinal–transverse shear modulus G_{zy} was obtained from nanoindentation measurements.

3.2 Three-dimensional reconstruction and microstructure characterization

A cylindrical sample with a diameter of 0.8 mm and height of 1 mm was prepared from a defect-free part of a jujube branch cross-section (five valid samples for each part for a total of 25 samples). X-ray scanning at a resolution of 0.618 μm resolution and image analysis procedures were performed using a NanoVoxel 3000 Industrial CT to acquire two-dimensional grayscale images for reconstructing microstructural visualization models. A grayscale image with a size of 1000 × 1000 pixels was selected for feature segmentation, noise reduction and other processing to obtain the microstructural visualization model (Fig. 3a, 3b). Three-dimensional microstructural reconstructions were performed using Avizo 9.0 software to obtain 3D visualization models in the different branch positions (Fig. 3c).

The mechanical behaviour of heterogeneous materials can be strongly influenced by their structural and material characteristics [27]. In wood processing, properties such as fibre orientation, density, and moisture content can significantly affect cutting behaviour [28]. Therefore, the microstructural components of the jujube branches were quantitatively characterized in the present study. In this study, the threshold image was binarized using image analysis software

ImageJ 1.80, and the binary images of different components were obtained (Fig. 3d). Based on the binary image results, the characteristics of the microscopic components were quantified, including porosity, component ratio, cell wall thickness, and distribution direction. Five two-dimensional CT images were analyzed at each position, giving a total of 25 valid images.

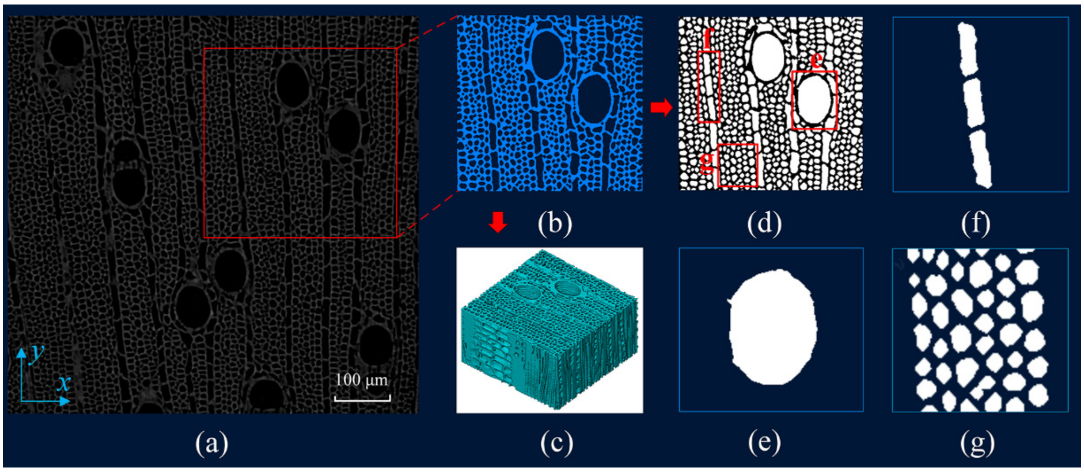

Fig. 3 Three-dimensional reconstruction and quantitative analysis of microstructure: (a) grayscale microstructure images; (b) threshold segmentation images; (c) visualization models; (d) binary inversion images of the cell wall; (e) vessels; (f) rays; (g) fibers

3.3 Analysis of mechanical properties of the multi-scale model

Finite element simulations are widely used to evaluate the influence of material properties and anisotropy on mechanical response, while multiscale models can be used to relate microstructural features to macroscopic equivalent properties [29, 30]. A representative volume element (RVE) was extracted from the visualization model to represent the microstructure. The elastic constants were obtained from stress and strain data in the linear elastic stage of the biomass-stalk microstructure. A uniaxial displacement load was applied to the representative volume element as shown in Eq. 3, and the equivalent macroscopic mechanical properties were then obtained using Eqs. 4 and 5.

$$u_i^{j+} - u_i^{j-} = \bar{\varepsilon}_i \left(x_k^{j+} - x_k^{j-} \right) \quad (3)$$

where u is the displacement. $j+$ and $j-$ are the positive and negative directions of the coordinate axis, respectively. $\bar{\varepsilon}_i$ is the average equivalent strain in the i-direction. x_k is the coordinate of any point on the representative volume element.

$$\overline{\sigma_{ij}} = \frac{1}{V}\int_V \sigma_{ij}\, dV, \qquad \overline{\varepsilon_{ij}} = \frac{1}{V}\int_V \varepsilon_{ij}\, dV \quad (4)$$

where $\overline{\sigma_{ij}}$ is the macroscopic equivalent stress. V is the volume of the representative volume element. $\overline{\varepsilon_{ij}}$ is the macroscopic equivalent strain.

$$E_i = \frac{\bar{\sigma}_i}{\bar{\varepsilon}_i}, \qquad \mu_{ij} = -\frac{\bar{\varepsilon}_i}{\bar{\varepsilon}_j}, \qquad G_{ij} = \frac{\bar{\tau}_{ij}}{\gamma_{ij}} \quad (5)$$

To maintain consistent microstructural porosity, representative volume units (35 × 35 × 35 μm) were extracted from different positions using the Avizo 9.0 visualization model (Fig. 4a, 4b). The average porosity of 1-5 sampling positions was 45.89 %, 48.45 %, 51.49 %, 53.82 %, and 56.17 %, respectively. Meanwhile, the plane where the points O', P' and Q' are located was defined as the main plane of the representative element, and the secondary plane was parallel to the main plane (Fig. 4c).

The microstructure of jujube branches is characterized by its porosity and non-uniformity. The application of appropriate boundary conditions in RVE-based multiscale models is important for determining the effective mechanical properties of heterogeneous microstructures [31-33]. Fixed displacement boundary conditions are more suitable for determining the elastic and viscoelastic behavior of non-uniform structures compared with periodic and mixed boundary conditions [34-35]. The elastic modulus of the plant stalk is approximately the same in tension and compression, and the stiffness characteristics are approximately symmetric [34]. Therefore, the constraint equations of representative volume elements under uniaxial compression and shear displacement loads were established to analyze the multi-scale mechanical properties of the microstructure (Tables 1 and 2).

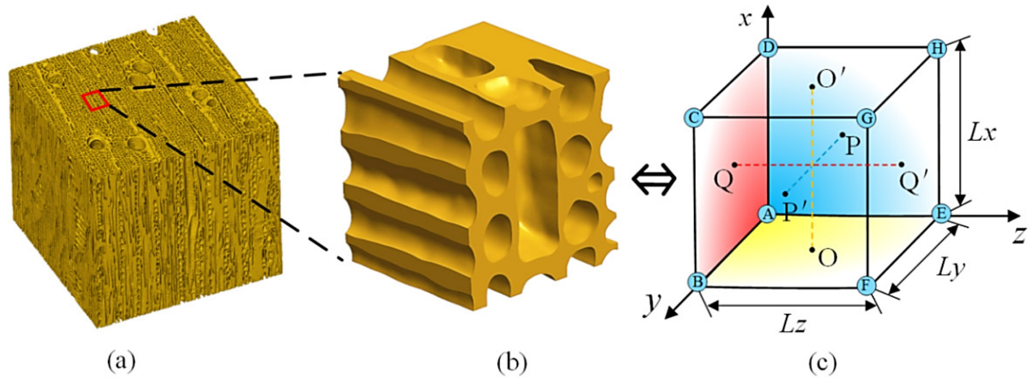

Fig. 4 Example of a representative volume element: (a) visual stereo model; (b) representative volume element; (c) simplified schematic diagram of representative volume element

Table 1 Constraint equations of tensile or compressive loads ($\varepsilon_x \neq 0$, $i = x$, ε_y, ε_z, γ_{zy}, $\gamma_{yz} = 0$)

Nodes on faces	Nodes on edges	Nodes on vertices
$u_i^{CDHG} - u_i^{ABFE} - I_x\varepsilon_x = 0$	$u_i^{CG} - u_i^{AE} - L_x\varepsilon_x = 0$	$u_i^G - u_i^A - L_x\varepsilon_x = 0$
$u_i^{BCGF} - u_i^{ADHE} = 0$	$u_i^{DH} - u_i^{BF} - L_x\varepsilon_x = 0$	$u_i^c - u_i^E - L_x\varepsilon_x = 0$
$u_i^{EFGH} - u_i^{ABCD} = 0$	$u_i^{GH} - u_i^{AB} - L_x\varepsilon_x = 0$	$u_i^F - u_i^D + L_x\varepsilon_x = 0$
	$u_i^{CD} - u_{1i}^{FE} - L_x\varepsilon_x = 0$	$u_i^H - u_i^B - L_x\varepsilon_x = 0$
	$u_i^{BC} - u_i^{FE} = 0$	
	$u_i^{FG} - u_i^{AD} = 0$	

Table 2 Constraint equations for shear loading ($\gamma_{zy} \neq 0$, $i \neq j$; ε_x, ε_y, ε_z, $\gamma_{yz} = 0$)

Nodes on faces	Nodes on edges	Nodes on vertices
$u_i^{CDHG} - u_i^{ABFE} = 0$	$u_i^{CG} - u_i^{AE} - L_y\gamma_{zy} = 0$	$u_i^G - u_i^A - L_y\gamma_{zy} = 0$
$u_i^{BCGF} - u_i^{ADHE} = 0$	$u_i^{BF} - u_i^{DH} - L_y\gamma_{zy} = 0$	$u_i^C - u_i^E + L_y\gamma_{zy} = 0$
$u_i^{EFGH} - u_i^{ABCD} - L_y\gamma_{zy} = 0$	$u_i^{GH} - u_i^{AB} = 0$	$u_i^F - u_i^D - L_y\gamma_{zy} = 0$
	$u_i^{CD} - u_i^{FE} = 0$	$u_i^B - u_i^H + L_y\gamma_{zy} = 0$
	$u_i^{BC} - u_i^{EH} + L_y\gamma_{zy} = 0$	
	$u_i^{FG} - u_i^{AD} - L_y\gamma_{zy} = 0$	

In Table 1, u is the uniaxial displacement in different directions. L is the side length of the representative volume element. ε_i is the positive strain in i-direction, $i = x, y, z$.

In Table 2, γ_{ij} is the shear strain in the ij-plane, $i \neq j$. To obtain the equivalent mechanical properties of the microstructure, the finite element analysis software Abaqus 6.14 was used for tetrahedral mesh generation and finite element simulation of representative volume elements. Using the fixed-displacement boundary conditions defined in Tables 1 and 2, the displacement degrees of freedom along the main plane of the representative volume element were constrained in Abaqus. Then, the equivalent mechanical properties of the microstructure were predicted by applying a uniaxial displacement load to reference point A (Fig. 5a, 5b). According to the multi-scale finite element simulation results, the stress-strain values of the reference point were extracted under the condition of displacement u = 0.001 mm (that is, the compression and shear strains were both 0.029). The macro-equivalent mechanical properties of the microstructure under compression and shear loads could be calculated using Eq. 5.

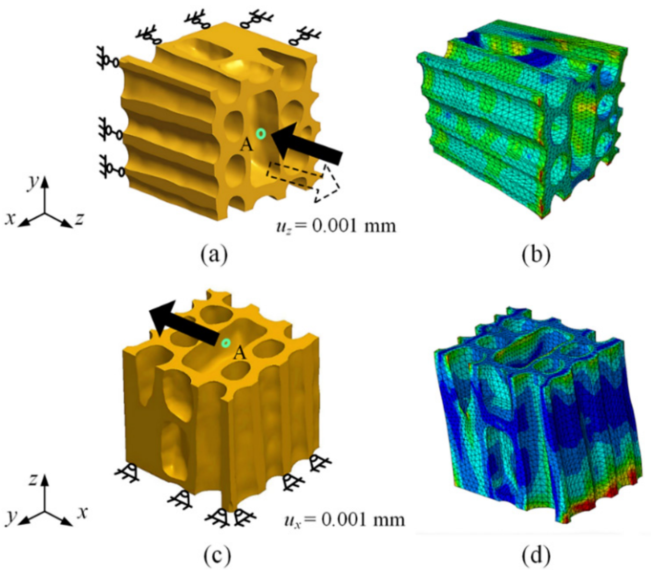

Fig. 5 Finite element simulation of multi-scale model: (a) boundary conditions of a tensile or compressive load; (b) compression mechanical properties; (c) boundary conditions of a shear load; (d) shear mechanical properties

4. Results and discussion

The differences in the physical and mechanical properties of jujube branch microstructures are the underlying reasons for variable macroscopic properties [35]. Therefore, exploring the effects of microstructural parameters on the mechanical properties of jujube branches is important for selecting a reasonable pruning position and cutting wedge angle. According to Table 3, there were significant differences in mechanical properties among different positions, and the mechanical properties decreased gradually from the base to the tip of jujube branches.

Table 3 Mechanical properties of cell wall and jujube branch

Positions	Micromechanical properties				Macroscopic mechanical properties				
	E_z* (MPa)	E_y* (MPa)	G_{xy}* (MPa)	G_{zy}* (MPa)	E_z (MPa)	E_x (MPa)	E_y (MPa)	G_{zy} (MPa)	G_{zx} (MPa)
1	9003.00	1333.78	537.81	606.26	4241.24	368.21	424.48	169.76	67.71
2	8575.50	1270.44	512.28	577.47	3853.62	287.97	400.00	162.14	65.53
3	7833.00	1160.44	467.92	527.47	3000.69	168.62	311.90	133.41	52.94
4	6847.50	1014.44	409.05	461.11	2773.28	188.90	310.76	112.03	46.77
5	6460.50	957.11	385.93	435.05	1947.38	150.03	241.52	90.34	39.06

Wood cell walls exhibit pronounced mechanical anisotropy, with the longitudinal elastic modulus being higher than the transverse elastic modulus and the axial shear modulus being higher than the transverse shear modulus [36, 37]. A similar directional dependence was observed in the present jujube branch and cell-wall models. Taking the micro-mechanical properties as an example, $G_{zy}* > G_{xy}*$ and $E_y* < E_z*$. The cell-wall mechanical properties are greater than the corresponding macroscopic properties of the jujube branch, such as $E_z*> E_z$, $E_x*> E_x$, etc. This difference is related to microstructural features, such as porosity, cell wall thickness, and stiffness, which can increase or decrease the macroscopic mechanical properties [38-39]. The quantitative microstructural results are shown in Fig. 6.

In Table 3, E_i* is the elastic modulus of the cell wall in different directions, MPa. G_{ij}* is the shear modulus, $i \neq j$, MPa. μ_{ij}* is the Poisson's ratio of the cell wall, $i \neq j$. The two-dimensional microstructural images were quantitatively analyzed and characterized, as shown in Fig. 6. Porosity gradually increases from the base to the tip of the jujube branches (Fig. 6a). The volume proportions of each micro-component vary little among branch positions, whereas the proportions of different components within each position differ substantially. Wood fibers are the main component, followed by rays and vessels (Fig. 6b). The quantitative analysis results reveal that porosity strongly influences the stalk mechanical properties with different contributions from each micro-component. The cell wall is thickest in the vessel tissue followed by the xylem ray and wood fiber, and the cell wall thickness of each component gradually decreases with increasing sampling height (Fig. 6c). In addition, the cell arrangement shows a characteristically random distribution, but the spatial distribution of different cell types shows certain regularities (Fig. 3a). Fig. 6d shows that the distribution direction of the wood fiber and vessel tissue is approximately parallel to the branch growth direction, whereas the distribution of xylem ray cells is approximately perpendicular. Wood fiber is the main microstructural component, accounting for 56.35-63.94 % [40]. Fiber cells are nearly parallel to the growth direction of the jujube branch, which makes the longitudinal mechanical properties much higher than the transverse mechanical properties (Table 3). The ray cells in the transverse plane are the primary reason for the differences in mechanical properties between x- and y-directions.

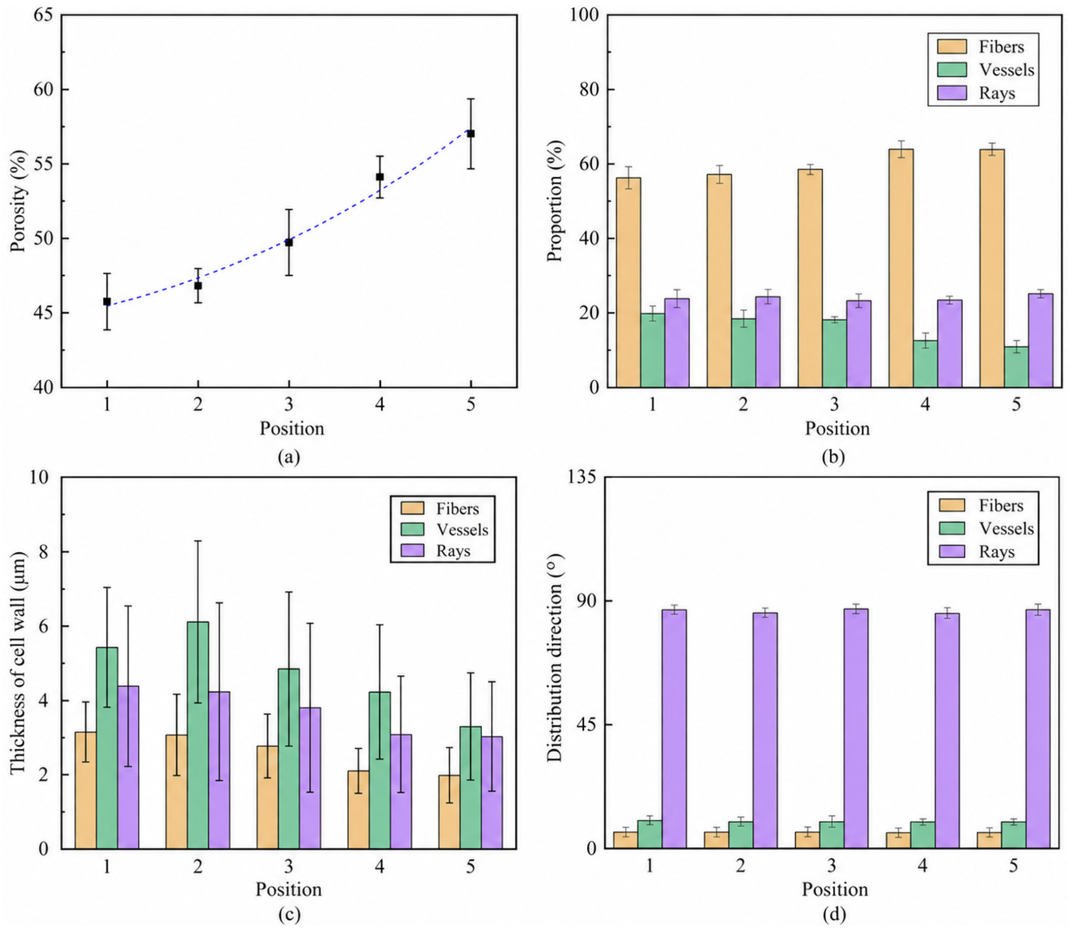

Fig. 6 Quantitative analysis results of microstructure: (a) porosity; (b) proportion of different components; (c) cell wall thickness; (d) direction of the cell distribution

To systematically characterize regional variations in mechanical behavior, multi-scale finite element simulations were performed across five jujube branch samples. Displacement-controlled loading was applied incrementally from u = 0 mm to u = 0.029 mm in steps of Δu = 0.001 mm; at each displacement increment, three to four independent simulations were executed to ensure numerical robustness. Stress and strain values were extracted at predefined reference points, yielding 100 data points per sample and a total of 500 data points across all samples. Microstructural parameters, including porosity, moisture content, and cell wall thickness, were subjected to one-way ANOVA and Tukey's post-hoc multiple comparisons using SPSS 25.0 (Tables 4 and 5). Results revealed no statistically significant differences (p > 0.05) for some adjacent comparisons (e.g., Positions 1 vs. 2 or 4 vs. 5), whereas significant differences (p < 0.01) were observed for several other comparisons–particularly in porosity, moisture content, and cell wall thickness–indicating longitudinal heterogeneity in the microstructure.

Table 4 Results of one-way ANOVA

Positions	Porosity (%)		Cell wall thickness (μm)		Water content (%)		Density (kg m^{-3})	
	M	*SD*	*M*	*SD*	*M*	*SD*	*M*	*SD*
1	45.76	1.94	3.15	0.81	35.50	1.77	828	0.036
2	46.83	1.15	3.07	1.09	36.43	1.5	819	0.034
3	49.73	2.22	2.77	0.87	38.10	1.79	799	0.038
4	54.13	1.39	2.11	0.6	40.29	1.92	787	0.031
5	57.02	2.35	1.99	0.74	41.15	2.11	776	0.034
F	33.31		127.74		43.85		9.66	
p	1.72E-8**		3.48E-94**		1.23E-22**		8.31E-7**	

Table 5 Multiple comparison results of the microstructure

Positions	Other positions	Porosity (%)		Cell wall thickness (μm)		Water content (%)		Density (kg m^{-3})	
		D	*p*	*D*	*p*	*D*	*p*	*D*	*p*
1	2	1.07	0.439	0.08	0.209	0.93	0.077	9	0.396
	3	3.97	0.004**	0.38	7.68E-9**	2.60	2E-6**	29	0.005**
	4	8.37	9.16E-7**	1.04	1.75E-50**	4.79	1.01E-15**	41	6.4E-5**
	5	11.26	8.62E-9**	1.16	2.04E-64**	5.65	1.09E-19**	52	5.61E-7**
2	3	2.90	0.023	0.30	1.5E-5**	1.67	0.002**	20	0.051
	4	7.30	5E-5**	0.96	3.01E-40**	3.86	1.38E-11**	32	0.002**
	5	10.19	3.57E-8**	1.08	5.41E-52**	4.72	1.96E-15**	43	2.5E-5**
3	4	4.40	0.001**	0.66	9.27E-21**	2.19	4.5E-5**	12	0.208
	5	7.29	0.005**	0.78	3.63E-29**	3.05	3.50E-8**	23	0.017*
4	5	2.89	0.024	0.12	0.104	0.86	0.100	11	0.254

In Table 4, *M* is the mean value. *SD* is the standard deviation. *F* is the F-statistic. *p* is the p-value (Note: * indicates significant, $p < 0.05$; ** indicates highly significant, $p < 0.01$).

In Table 5, *D* is the difference between the means. Plant stalk microstructures are closely related to their mechanical properties. During crushing or shearing operations, jujube branches are mainly subjected to compressive and shear loads. According to the finite element simulation analysis (Table 3), the ratio of micromechanical properties to macro-equivalent mechanical properties (R_m) was defined as an index to evaluate the reduction/enhancement effect of various factors on the equivalent mechanical properties. The transverse elastic modulus and shear modulus are important indices to evaluate the compression and shear capacity of materials. The equivalent mechanical properties in the y-direction and zy-plane of jujube branches were slightly greater than those in the x-direction and zx-plane (that is, $E_y > E_x$, $G_{zy} > G_{zx}$), as shown in Table 3. The calculated ratios are shown in Fig. 7.

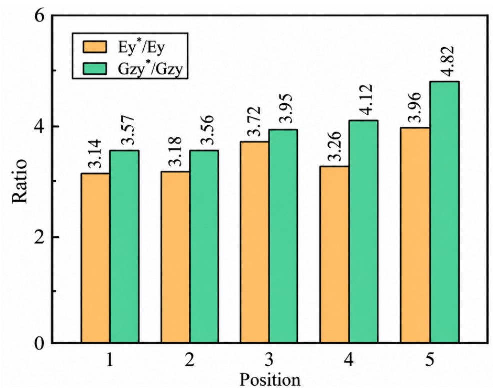

Fig. 7 Ratio of mechanical properties

The transverse elastic modulus E_y and shear modulus G_{zy} were therefore selected to calculate the reinforcement or reduction ratio of each factor on the equivalent mechanical properties (Fig. 7). According to the analysis in Fig. 7, the mechanical properties of the cell wall are greater than the macro-equivalent mechanical properties [32, 36]. This indicates that the microstructure reduces the effective mechanical properties relative to the solid cell wall. To evaluate the strength of the association between each factor and the reduction/enhancement of the equivalent mechanical properties, the correlation between each factor and R_m was analyzed using SPSS software (Table 6). According to the results in Table 6, the correlation between each factor and R_m is statistically significant ($p < 0.01$). For example, porosity shows the strongest correlation with the mechanical property ratio of G_{zy}^*/G_{zy}, ($|r| = 0.891$), followed by moisture content ($|r| = 0.710$) and density ($|r| = 0.461$), while cell wall thickness shows the weakest correlation ($|r| = 0.458$). Porosity, moisture content, and R_m are all positively correlated ($r > 0$), which shows that higher porosity and water content are associated with larger R_m, and lower equivalent mechanical properties. Density and cell wall thickness are negatively correlated with R_m ($r < 0$). As density and cell wall thickness increase, the reduction in equivalent mechanical properties becomes smaller (Table 6).

Table 6 Correlations between factors and mechanical property ratios.

Ratio	Coefficient	Factors			
		Porosity	Cell wall thickness	Moisture content	Density
E_y^*/E_y	r	0.648	-0.315	0.519	-0.370
	p	4.67E-4**	1.04E-36**	5.49E-36**	2.2E-5**
G_{zy}^*/G_{zy}	r	0.891	-0.458	0.710	-0.461
	p	2.41E-9**	2.26E-80**	1.77E-20**	6.40E-8**

In Table 6, r is the correlation coefficient. Differences in microstructure lead to directional differences in the shear mechanical properties of jujube branches. Previous studies have shown that cutter geometry, including the cutting-edge angle, can influence the cutting force and stress distribution during material removal [41, 42]. During cutting of jujube branches, the cutting direction (transverse direction) of the cutter is perpendicular to the stem growth direction (Fig. 8a). The angle between the cutting direction and cutting wedge surface of the jujube branch is called the wedge angle α (θ is the angle between the direction of the cutting force and the growth direction) [43]. The tool tip point T is taken as an example, where T' is the point at which the balancing reaction force acts (Fig. 8b). The tangential component force F_t of the cutting force F on the wedge surface effectively cuts the fibers, while the normal component F_n could increase the cutting displacement of the wedge surface. By decomposing F_t into a transverse component F_{zy} and longitudinal component F_{yz}, the former is considered the main force for cutting fibers. The selection of a smaller transverse cutting force and reasonable wedge angle is therefore the key to reducing cutting energy consumption.

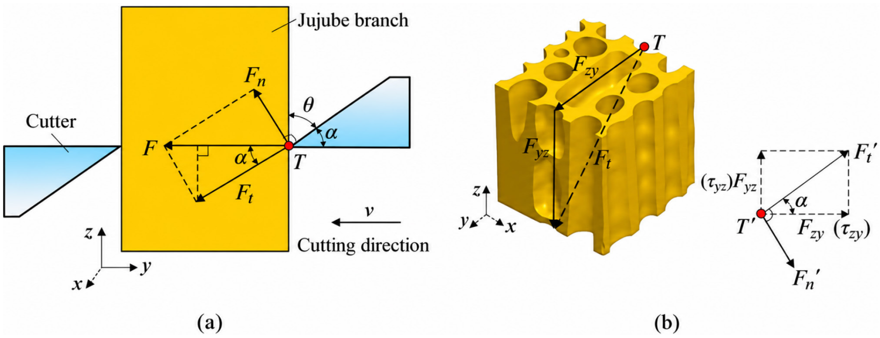

Fig. 8 Shear force diagram of a jujube branch: (a) cutter wedge angle; (b) shear force analysis of a representative volume element

$$\alpha = \arctan\left(\frac{F_{zx}}{F_{zy}}\right) = \arctan\left(\frac{\tau_{zx}}{\tau_{zy}}\right) = \arctan\left(\frac{G_{zx}}{G_{zy}}\right) \tag{6}$$

According to the analysis in Fig. 8b, the component forces F_{zy} and F_{yz} of the wedge cutting force F_t in the transverse and longitudinal directions determine the cutter wedge angle, as shown in Eq. 6. However, to avoid the influence of jujube branch diameter, the wedge angle was calculated using the shear stresses in Eq. 6. According to Eqs. 5 and 6, under the same shear strain conditions ($\gamma_{zy} = \gamma_{yz} = 0.029$), the ratios of shear stress to shear modulus are equal in the two directions, that is, the ratio of the longitudinal shear modulus to the transverse shear modulus determines the cutter wedge angle. The cutter wedge angle range can be calculated according to the shear moduli at the different positions, giving α = 21.65-23.36° (Fig. 9). This variation is attributed to differences in mechanical properties among branch positions. The shear mechanical properties at the base of the jujube branch are higher than in other parts. The recommended wedge angle at the base of the jujube branch is α = 21.75°.

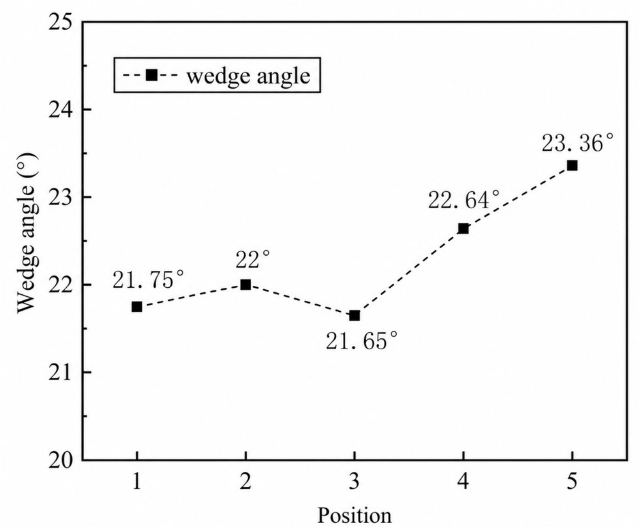

Fig. 9 Wedge angle at different positions

5. Conclusion

Significant differences in porosity, cell wall thickness, density, and water content were observed among several branch positions, while some adjacent comparisons were not significant ($p > 0.05$). Higher porosity and water content are associated with lower equivalent microstructural mechanical properties, with porosity showing the stronger association. The wedge angle of jujube pruning cutters mainly depends on the ratio of longitudinal to transverse shear modulus, and the recommended wedge angle is α = 21.75°. However, because this study was based on simulations and did not include physical cutting tests, the recommended angle requires experimental validation.

References

[1] Zheng, Z., Liu, Y., Dong, J., Zhao, P., Qiao, Y., Sun, S., Huang, Y. (2024). A novel jujube tree trunk and branch salient object detection method for catch-and-shake robotic visual perception, *Expert Systems with Applications*, Vol. 251, Article No. 124022, doi: 10.1016/j.eswa.2024.124022.

[2] Zheng, Z., Hu, Y., Li, X., Huang, Y. (2023). Autonomous navigation method of jujube catch-and-shake harvesting robot based on convolutional neural networks, *Computers and Electronics in Agriculture*, Vol. 215, Article No. 108469, doi: 10.1016/j.compag.2023.108469.

[3] Muthukumaran, S., Sivaramakrishnan, R. (2019). Optimal path planning for an autonomous mobile robot using dragonfly algorithm, *International Journal of Simulation Modelling*, Vol. 18, No. 3, 397-407, doi: 10.2507/IJSIMM18(3)474.

[4] Hu, Y., Zheng, Z., Yu, C., Feng, J., Qiao, Y. (2024). Vibration response characteristics of jujube trees based on finite element method and structure-from-motion, *Scientia Horticulturae*, Vol. 331, Article No. 113125, doi: 10.1016/j.scienta.2024.113125.

[5] Zheng, Z., Hu, Y., Dong, J., Zhao, P., Liu, Y., Jiang, X., Qiao, Y., Sun, S., Huang, Y. (2024). Characterising vibration patterns of winter jujube trees to optimise automated fruit harvesting, *Biosystems Engineering*, Vol. 248, 255-268, doi: 10.1016/j.biosystemseng.2024.11.004.

[6] Zeng, F., Yang, B., Zhao, M., Xing, Y., Ma, Y. (2022). MASANet: Multi-angle self-attention network for semantic segmentation of remote sensing images, *Tehnički Vjesnik – Technical Gazette*, Vol. 29, No. 5, 1567-1575, doi: 10.17559/TV-20220421142959.

[7] Aydin, I., Sevi, M., Akin, E., Güçlü, E., Karaköse, M., Aldarwich, H. (2023). A deep learning-based hybrid approach to detect fastener defects in real-time, *Tehnički Vjesnik – Technical Gazette*, Vol. 30, No. 5, 1461-1468, doi: 10.17559/TV-20221020152721.

[8] Yang, C., Dimyati, K., Mohamad, M. (2024). Detection and classification of railway track surface erosion-caused holes and scratches defects based on YOLOv5s, *Tehnički Vjesnik – Technical Gazette*, Vol. 31, No. 4, 1288-1296, doi: 10.17559/TV-20240422001485.

[9] Peng, F., Zheng, H., Lu, S., Shi, Z., Liu, X., Li, L. (2019). Growth model and visualization of a virtual jujube tree, *Computers and Electronics in Agriculture*, Vol. 157, 146-153, doi: 10.1016/j.compag.2018.12.045.

[10] Ma, X., Zhang, F., Luo, H., Guo, G. (2024). Water shortage detection of jujube trees based on spectral technology and random forest classifier integrated with fractal theory, *Industrial Crops and Products*, Vol. 216, Article No. 118729, doi: 10.1016/j.indcrop.2024.118729.

[11] Mahmood, A., Tiwari, A.K., Singh, S.K. (2024). Maturity grading of jujube for industrial applications harnessing deep learning, *Engineering Computations*, Vol. 41, No. 5, 1171-1184, doi: 10.1108/EC-08-2023-0426.

[12] Zhang, L., Chen, Y., Guo, X., Li, Y., Chen, C., Zou, Y., Zhang, X., Hu, J. (2024). Abnormal phenotypic defects detection of jujube using explainable machine learning enhanced computer vision, *Journal of Food Science*, Vol. 89, No. 11, 7713-7728, doi: 10.1111/1750-3841.17393.

[13] Qiu, X., Xing, W., Que, Y., Lu, G. (2025). Summer pruning in apple trees is an advisable cultural practice that promotes bud differentiation and improves fruit quality: A literature review, *PeerJ*, Vol. 13, Article No. e20229, doi: 10.7717/peerj.20229.

[14] Tong, S., Wang, J., Zhang, J., Liu, L., Wang, Y., Kang, F. (2026). An apple tree pruning robot system based on branch segmentation and decision-making control, *Artificial Intelligence in Agriculture*, Vol. 16, No. 2, 1025-1040, doi: 10.1016/j.aiia.2026.04.005.

[15] Liu, J., Han, X., Mulongoti, C., Ma, Z., Yao, X., Zhuang, Q., Castro-García, S., Du, X. (2025). Vibration dynamics of pruned canopy: Investigating the impact of excitation trajectories on fruit-tree system response, *Biosystems Engineering*, Vol. 257, Article No. 104236, doi: 10.1016/j.biosystemseng.2025.104236.

[16] Cao, Y., Wang, N., Wu, B., Zhang, X., Wang, Y., Xu, S., Zhang, M., Miao, Y., Kang, F. (2025). A novel adaptive cuboid regional growth algorithm for trunk-branch segmentation of point clouds from two fruit tree species, *Agriculture*, Vol. 15, No. 14, Article No. 1463, doi: 10.3390/agriculture15141463.

[17] Win, N.M., Park, J., Kim, S., Lee, Y., Do, V.G., Kwon, J.-G., Kwon, S.-I., Yoo, J., Kang, I.-K., Kweon, H.-J. (2025). Effects of mechanical pruning on tree growth, yield, and fruit quality of 'Arisoo' apple trees, *Agriculture*, Vol. 15, No. 20, Article No. 2118, doi: 10.3390/agriculture15202118.

[18] Chen, Y.Y., Fu, Y.X., Zhang, B., Fu, W., Shen, C.J. (2022). Path planning of the fruit tree pruning manipulator based on improved RRT-Connect algorithm, *International Journal of Agricultural and Biological Engineering*, Vol. 15, No. 2, 177-188, doi: 10.25165/j.ijabe.20221502.6249.

[19] Liu, G., Boom, B., Slob, N., Durodié, Y., Nowé, A., Vanderborght, B. (2026). Automated behavior planning for fruit tree pruning via redundant robot manipulators: Addressing the behavior planning challenge, *IEEE Robotics & Automation Magazine*, Vol. 33, No. 2, 65-75, doi: 10.1109/MRA.2025.3559797.

[20] Gindl, W., Schöberl, T. (2004). The significance of the elastic modulus of wood cell walls obtained from nanoindentation measurements, *Composites Part A: Applied Science and Manufacturing*, Vol. 35, No. 11, 1345-1349, doi: 10.1016/j.compositesa.2004.04.002.

[21] Huang, Y., Fei, B., Wei, P., Zhao, C. (2016). Mechanical properties of bamboo fiber cell walls during the culm development by nanoindentation, *Industrial Crops and Products*, Vol. 92, 102-108, doi: 10.1016/j.indcrop.2016.07.037.

[22] Keryvin, V., Lan, M., Bourmaud, A., Parenteau, T., Charleux, L., Baley, C. (2015). Analysis of flax fibres viscoelastic behaviour at micro and nano scales, *Composites Part A: Applied Science and Manufacturing*, Vol. 68, 219-225, doi: 10.1016/j.compositesa.2014.10.006.

[23] Stevanic, J.S., Salmén, L. (2009). Orientation of the wood polymers in the cell wall of spruce wood fibres, *Holzforschung*, Vol. 63, No. 5, 497-503, doi: 10.1515/HF.2009.094.

[24] Stubbs, C.J., Sun, W., Cook, D.D. (2019). Measuring the transverse Young's modulus of maize rind and pith tissues, *Journal of Biomechanics*, Vol. 84, 113-120, doi: 10.1016/j.jbiomech.2018.12.028.

[25] Malaga-Toboła, U., Łapka, M., Tabor, S., Niesłony, A., Findura, P. (2019). Influence of wood anisotropy on its mechanical properties in relation to the scale effect, *International Agrophysics*, Vol. 33, No. 3, 337-345, doi: 10.31545/intagr/110808.

[26] Malek, S., Gibson, L.J. (2017). Multi-scale modelling of elastic properties of balsa, *International Journal of Solids and Structures*, Vol. 113-114, 118-131, doi: 10.1016/j.ijsolstr.2017.01.037.

[27] Masood, A.A., Ali, A., Madhu, P., Yashas Gowda, T.G., Jeevan, T.P., Sharath, B.N. (2024). Characterizing the effects of SiC and Al_2O_3 on the mechanical properties of Al6082 hybrid metal matrix composites: An experimental and neural network approach, *Advances in Production Engineering & Management*, Vol. 19, No. 2, 281-292, doi: 10.14743/apem2024.2.507.

[28] Vievesis, M., Kujalavicius, Z., Keturakis, G., Gyliene, V., Jablonskyte, J. (2025). Impact of machining parameters on surface roughness in CNC hardwood milling: A multivariate approach, *Advances in Production Engineering & Management*, Vol. 20, No. 2, 191-204, doi: 10.14743/apem2025.2.535.

[29] Faisal, T.R., Hristozov, N., Western, T.L., Rey, A.D., Pasini, D. (2014). Computational study of the elastic properties of Rheum rhabarbarum tissues via surrogate models of tissue geometry, *Journal of Structural Biology*, Vol. 185, No. 3, 285-294, doi: 10.1016/j.jsb.2014.01.012.

[30] Sevšek, L., Vilkovský, S., Majerníková, J., Pepelnjak, T. (2024). Predicting the deep drawing process of TRIP steel grades using multilayer perceptron artificial neural networks, *Advances in Production Engineering & Management*, Vol. 19, No. 1, 46-64, doi: 10.14743/apem2024.1.492.

[31] Rosnitschek, T., Hueter, F., Alber-Laukant, B. (2020). FEM-based modelling of elastic properties and anisotropic sinter shrinkage of metal EAM, *International Journal of Simulation Modelling*, Vol. 19, No. 2, 197-208, doi: 10.2507/IJSIMM19-2-509.

[32] Saavedra Flores, E.I., Friswell, M.I. (2012). Multi-scale finite element model for a new material inspired by the mechanics and structure of wood cell-walls, *Journal of the Mechanics and Physics of Solids*, Vol. 60, No. 7, 1296-1309, doi: 10.1016/j.jmps.2012.03.007.

[33] Zhou, F., Huang, J., Liu, W., Deng, T., Jia, Z. (2019). Multiscale simulation of elastic modulus of rice stem, *Biosystems Engineering*, Vol. 187, 96-113, doi: 10.1016/j.biosystemseng.2019.09.003.

[34] Al-Zube, L., Sun, W., Robertson, D., Cook, D. (2018). The elastic modulus for maize stems, *Plant Methods*, Vol. 14, Article No. 11, doi: 10.1186/s13007-018-0279-6.

[35] Zhao, D., Shi, W., Xia, X., Tang, Y., Tao, J. (2020). Microstructural and lignin characteristics in herbaceous peony cultivars with different stem strengths, *Postharvest Biology and Technology*, Vol. 159, Article No. 111043, doi: 10.1016/j.postharvbio.2019.111043.

[36] Qing, H., Mishnaevsky, L. (2011). A 3D multilevel model of damage and strength of wood: Analysis of microstructural effects, *Mechanics of Materials*, Vol. 43, No. 9, 487-495, doi: 10.1016/j.mechmat.2011.05.007.

[37] Arzola-Villegas, X., Plaza, N.Z., Bechle, N.J., Wang, Y., Lakes, R., Stone, D.S., Jakes, J.E. (2025). Moisture-dependent transverse isotropic elastic constants of wood S2 secondary cell wall layers determined using nanoindentation, *Forests*, Vol. 16, No. 5, Article No. 712, doi: 10.3390/f16050712.

[38] Kovács, Á., Kerényi, G. (2019). Physical characteristics and mechanical behaviour of maize stalks for machine development, *International Agrophysics*, Vol. 33, No. 4, 427-436, doi: 10.31545/intagr/113335.

[39] Wójtowicz, T., Grabowska-Joachimiak, A., Zieliński, A. (2020). Analysis of morpho-anatomical stem properties determining its mechanical strength in selected rye cultivars, *International Agrophysics*, Vol. 34, No. 1, 123-131, doi: 10.31545/intagr/115096.

[40] Steele, J.H., Ifju, G., Johnson, J.A. (1976). Quantitative characterization of wood microstructure, *Journal of Microscopy*, Vol. 107, No. 3, 297-311, doi: 10.1111/j.1365-2818.1976.tb02450.x.

[41] Rabbani, H., Sohraby, N., Gholami, R., Jaliliantabar, F., Waismorady, A. (2015). Determination of mass density module, crush resistance coefficient and cutting efficiency of rose (Rosa Damascene Mill), *Scientia Horticulturae*, Vol. 190, 144-148, doi: 10.1016/j.scienta.2015.02.009.

[42] Ju, P. (2023). Optimizing rock breaking performance: The influence of chamfer on polycrystalline diamond compact (PDC) cutters, *Advances in Production Engineering & Management*, Vol. 18, No. 4, 417-433, doi: 10.14743/apem2023.4.482.

[43] Johnson, P.C., Clementson, C.L., Mathanker, S.K., Grift, T.E., Hansen, A.C. (2012). Cutting energy characteristics of *Miscanthus x giganteus* stems with varying oblique angle and cutting speed, *Biosystems Engineering*, Vol. 112, No. 1, 42-48, doi: 10.1016/j.biosystemseng.2012.02.003.